Thermal stability of artificial radiation-induced defects in kaolinite: Enhancing EPR dating protocol

Öykü Ataytür, Cécile Gautheron, Adriana Horbe, Thierry Allard

Thermal stability of artificial radiation-induced defects in kaolinite: Enhancing EPR dating protocol

Öykü Ataytür [a]*, Cécile Gautheron [b,c], Adriana Horbe [d], Thierry Allard [a]

[a]IMPMC, UMR, CNRS 7590, Sorbonne Université, 4 Place Jussieu,75005, Paris, France

[b] GEOPS, Univ. Paris-Sud, CNRS, Université Paris-Saclay, 91405, Orsay, France

[c] ISTerre, Univ. Grenoble Alpes, Univ. Savoie Mont Blanc, CNRS, IRD, IFSTTAR, 38041, Grenoble, France

[d] Instituto de Geociências, Universidade de Brasilia, Brazil

*oyku.ataytur@sorbonne-universite.fr

ABSTRACT

Kaolinite naturally contains radiation-induced electron defects in its structure induced by ionizing radiations and can be analyzed with electron paramagnetic resonance spectroscopy (EPR). They include the so-called A-center, which is crucial for geochronological applications due to its stability at the scale of geological periods. Indeed, previous studies have substantiated the thermal stability of naturally occurring A-centers in kaolinite through annealing experiments. However, the stability of artificially created A-centers, which are used to determine paleodose through calibration via irradiation experiments and subsequent dating of kaolinite formation, still needs to be more adequately specified to confirm their relevance. Therefore, this research probed the thermal stability of A-centers produced by ionizing 1.5 MeV He^+ beams in two samples, i.e., the reference KGa-2 and a very disordered lateritic soil kaolinite. Heating experiments showed that the annealing of irradiated samples at 250°C was relevant to determining A-center concentration. Second, the annealing of artificial A-centers at higher temperatures was found to be a second-order process, as for natural A-centers. Annealing parameters such as

activation energy (2-2.6 eV) were determined with estimates of half-life at 300K, which was found to be > 10^{12} years for natural and artificial A-centers. Thus, the parameters for artificial A-centers are consistent with the thermal annealing behavior of their natural counterparts. These new findings affirm that artificially generated A-centers mimic natural ones in terms of EPR spectra and thermal stability, enhancing the reliability and precision of EPR dating methodologies used in kaolinite dating.

Keywords: Kaolinite, Radiation-induced defects, A-center, Thermal stability, EPR dating

1. Introduction

Kaolinite, a ubiquitous clay mineral at the Earth's surface, is a crucial archive for deciphering the complex sequence of geological, soil, or paleoclimatic transformations over time (Murray, 1988; 2007; Balan et al., 2014; Mathian et al., 2019; 2020; 2022). Its structure exhibits a spectrum of various points or extended defects (Cases et al., 1982; Giese, 1988; Clozel et al., 1994), offering valuable insights into formation conditions and geological history. In particular, irradiation can induce radiation-induced defects, the influence of which on changes in material physicochemical properties, including specific surface area, cation exchange capacity, and mean layer charge, has been explored previously (Pushkareva et al., 2002; Plötze et al., 2003; Allard and Calas, 2009; Balan et al., 2011).

In this study, the investigation focuses on the Radiation-Induced defects (RIDs) present in all-natural kaolinite, which can be detected via the sensitive Electron Paramagnetic Resonance technique (EPR) (Angel et al., 1974; Meads and Malden, 1975; Cuttler, 1980). These early studies showed that these defects were identified as trapped positive holes on oxygen atoms of the kaolinite structure according to their g values, which are higher than g values for the free electron (g=2.0023). Four RIDs were differentiated according to their EPR signal, their symmetry, and the presence of a superhyperfine structure or not, namely A-, A',

B-, and H- centers (Allard et al., 2012). Some isochronal or isothermal annealing experiments demonstrated that these defects exhibit contrasting stabilities (Clozel et al., 1994). Furthermore, Goodman et al. (2016) proposed the existence of an additional radiation-induced defect known as the C-center, but its stability was not explored. This revealed that annealing kinetics of the most stable RID, the so-called A-center, was a second-order process and enhanced the knowledge of its activation energy (around 2 eV) and half-life, around 10^{12} years, as extrapolated at Earth's surface temperature (300 K). This defect is thus stable at the scale of geological periods and cumulates over time, providing various applications that are valuable for Earth science issues.

The RIDs represent signatures of radioactivity, first offered a perspective of tracing radionuclide migrations in the geosphere, thus by using kaolinite as an 'in situ dosimeter' (Muller et al., 1992; 1993; Ildefonse et al., 1990; Allard et al., 1994; Allard and Muller, 1998; Allard et al., 2007). In detail, this led to the determination of long-term losses or gains of radionuclides definitively recorded by the clay mineral and that were not revealed by geochemical approaches. The stable A-centers have been used as geochronometers, uncovering a succession of weathering events through their extensive chronology (Balan et al., 2005; Allard et al., 2012; 2018; 2020; Mathian et al., 2019; 2020; 2022). In particular, the study of kaolinites in lateritic soils has shown to be particularly elucidative. In those studies, the protocol for dating relies on artificial irradiations to simulate the effect of natural ionizing radiations and on the determination of the paleodose (dose rate that has affected the kaolinite since its formation). The age is then classically determined as the paleodose divided by the dose rate (Hennig and Grün, 1983). This methodology of EPR dating, when applied to clay minerals, has regularly improved, mainly through the fitting of dosimetry data and the corrections of the dose rate. Despite these efforts and their importance in reinforcing the EPR dating methodology of kaolinite, the relevance of artificial A-centers to simulate the natural ones remains undocumented. It is the central inquiry of the present study.

This study questioned whether artificially produced defects can correlate with the stability of their natural equivalents, thereby validating their use in dosimetry and subsequent dating of kaolinite. Regarding the widespread presence of kaolinites with variable crystallinity, this research compares two distinct samples: the reference kaolinite KGa-2 that has a medium degree of crystalline order (Pineau et al., 2022) and a soil kaolinite labeled PF2-50 from an Amazonian laterite which is strongly disordered (this study). Results of isothermal annealing kinetics at various temperatures (250°C, 350°C, 375°C, 400°C) are presented. Subsequently, the activation energy and half-life are determined and compared between natural A-centers and their artificial counterparts induced by He^+ ion-beam irradiations at efficient fluences.

2. Methods and Materials

2.1. Methods

2.1.1. Characterization of samples

XRD measurement was performed on a ground powder sample with a Panalytical Pro MPD equipped with an X'Celerator detector and Co-Kα_1 radiation (1.789010 Å). XRD patterns were recorded with a 2θ range of 3 to 110°, with step sizes of 0.017° and an acquisition time of 280 ms/step employing a fixed divergence slit with an angle of 0.5° and a fixed anti-scatter slit with an angle of 1° (i.e., height of 1.52 mm). They were used to determine crystalline order indices such as Hinckley, HI, and Liétard, LI, indices (Hinckey, 1962; Liétard, 1977; Pineau et al., 2022). Disoriented samples were prepared by filling a hollowed aluminum holder and gently smoothing over with a frosted glass slide.

EPR spectroscopy was employed using a Bruker EMX plus™ spectrometer operating at X-Band frequency (9.86 GHz) with a rectangular high-sensitivity resonator cavity. The EPR spectra were meticulously recorded under consistent conditions to ensure repeatability and accuracy. The setting was a microwave power of 40 mW, which is maximum intensity

just before the plateau of saturation (Figure S1), a modulation amplitude of 0.3 mT for RID spectra, 0.5 mT for total spectra, and a modulation frequency of 100 kHz.

Data were normalized according to the sample mass, receiver gain, and a constant resonant cavity-filling factor. In defining the EPR spectra, the so-called *g* factor of the signal was the main characteristic parameter determined from the resonance condition eq. 1:

$$h\,\nu = g\,\beta\,H_0 \qquad \text{[eq. 1]}$$

Where *h* is the Planck constant; *v* symbolizes the resonance frequency; *g* represents the Landé factor (the A-center signal exhibiting apparent axial anisotropy at X-band with $g_{//}$ and $g_{\perp}$ components), β stands for the Bohr magneton, and H_0 is the external magnetic field.

The crystalline disorder was assessed by the EPR Gaite index (Gaite et al.,1997), while the structural Fe^{3+} concentrations were measured according to the methodology established by Balan et al. (2000). The EPR spectrum of the structural trivalent iron comprises two signals, namely the Fe $_{(2)}$ one which corresponds to the well-ordered structure of kaolinite, while the Fe $_{(1)}$ one is related to its disordered structure (Balan et al., 1999). The Gaite index is a unitless measurement of the width of the isolated peak around *g*=9 divided by its distance to the next intense Fe $_{(2)}$ peak. In natural samples, it varies roughly between 3 (ordered end-member) and 17 (disordered end-member). The concentration of diluted structural trivalent iron is measured on the most intense part of its spectrum (including Fe $_{(1)}$ and Fe $_{(2)}$) by double integration after removing the baseline, as shown in Fig. S2 and calibrating to the spectrum of a reference kaolinite already quantified in a former study (Balan et al., 2000). Concentrations of RIDs values were approximated by measuring the peak amplitude of the EPR spectra within the 330-370 mT range corresponding to the perpendicular component, expressing the results in arbitrary units proportional to the spin concentration per gram. Acknowledging errors on potential variables such as mass, height in the tube, and apparatus deviation, a ±10% total error was applied to the concentrations.

2.1.2. Irradiation experiments

The samples were irradiated with a He^+ beam using the Tandem ARAMIS particle accelerator (IJCLab, Orsay, France) with fluences of 10^{12} and 10^{13} ions/cm² for the 250°C heating experiment and 10^{13} ions/cm² for the higher temperatures. ARAMIS is a linear accelerator providing high-energy ion beams applied to relatively high amounts of irradiated material. Before irradiation, each sample was carefully deposited from an aqueous suspension on stainless steel plates, achieving a thickness of 4 µm. This specific thickness corresponds to the penetration range of 1.5 MeV He^+ ions in kaolinite according to the SRIM Monte Carlo code for Stopping and Range of Ions in Matter (Ziegler et al., 2010), which calculates the parameters of the impact of particles in solids.

2.1.3. Annealing experiments

2.1.3.1. Annealing of unstable defects

The first investigation focussed on the relevance of the 250°C, 2h treatment to remove unstable defects after artificial irradiations to check if these conditions ensure a stable resulting concentration of A-centers. Among unstable defects are B and A' centers, as inferred from isochronal heating experiments (Clozel et al., 1994; Allard et al., 1994). Measurements were systematically carried out at specific time intervals: 2h, 5h, 27h, 72h, 144h, and 408h. This experiment was conducted on the KGa-2 kaolinite irradiated at two fluences, 10^{12} and 10^{13} ions/cm^2, at which it is known that a significant amount of artificial A-centers can be produced (Allard et al., 1994; Allard and Muller, 1998).

2.1.3.2. Isothermal annealing of A-centers

All kaolinite samples were exposed to predetermined temperatures of 350°C, 375°C, and 400°C. EPR characterizations were performed at specified durations (18h, 24h, 48h, 72h, 96h, 120h) known to induce measurable A-center annealing on natural and artificially

irradiated samples. Prior to isothermal annealing, preliminary annealing at 250°C for 2h was performed to remove unstable defects on artificially irradiated samples (Allard et al., 1994).

2.2. Materials

2.2.1 Mineralogical characterization of the two kaolinite samples

Two kaolinite samples, namely KGa-2 and PF2-50, were analyzed. KGa-2 is an internationally referenced kaolinite from Georgia, USA, known for its poorly crystalline structure. This pure clay standard, housed in the Clay Minerals Society mineral repository, primarily comprises kaolinite with trace amounts of anatase (Van Olphen and Fripiat, 1979). PF2-50, sourced from laterite topsoil developed on the Alter do Chao sedimentary formation around 100 km north of Manaus, near Presidente Figueiredo, Amazonia, Brazil, exhibits a higher degree of structural disorder mainly due to a relatively high content of stacking faults. The sample used in this study was purified (see below) and predominantly consisted of kaolinite.

The degree of crystalline order was measured using X-ray diffraction (XRD) to determine the Hinckley and Liétard indices (Hinckley, 1962; Liétard, 1977) and using EPR to determine the Gaite disorder index (Gaite et al., 1997) together with the concentration of structural Fe^{3+} (Balan et al., 2000). The structural iron corresponds to Fe^{3+} substituting for Al^{3+} in the kaolinite structure. Only the diluted part of this population is quantitatively measured by EPR, not the iron potentially occurring as clusters.

2.2.2. Purification

The KGa-2 sample was used in the form provided by the CMS source repository. In contrast, the soil sample purification for EPR analysis was performed using the Mehra and Jackson (1965) deferration methodology. The PF2-50 sample, approximately 8 grams, was finely ground with an agate mortar and pestle. It was then subjected to at least three citrate-

dithionite-bicarbonate (CBD) treatment cycles to remove iron oxides. Deferration involved a 0.2 M sodium citrate dihydrate and 0.1 M sodium bicarbonate solution mixed with powdered soil and sodium hydrosulfite. The solution was heated to 80°C while stirring to ensure homogeneity. After reaction with DCB, the samples were rinsed with deionized water three times and centrifuged to extract the clay-sized particles, dominantly composed of kaolinite. As in all previous quantitative studies of RID in kaolinite, the objective of the deferration was to lower the contribution of iron oxides that are responsible for the baseline in the EPR spectrum and may interfere with the RID signal. Subsequently, the sample was checked by XRD and EPR. Only a small contribution of iron oxides remained in the EPR spectrum of the purified sample (which turned from reddish to white), which did not hinder the measurement of RID intensity, provided that a correction of the remaining baseline could be undertaken.

3. RESULTS AND DISCUSSION

3.1 Characterization of the samples

Table 1 presents the distinctive crystallinity of kaolinite samples KGa-2 and PF2-50. In terms of disorder, this partly reflects the diverse characteristics often found in lateritic profiles. KGa-2, with a Hinckley Index (HI) of 0.21, a Liétard Index (LI) of 0.68, and a Gaite index of 11.3, had a moderate degree of crystalline disorder.

Table 1. Characterization of Kaolinite Samples KGa-2 (Georgia, USA) and PF2-50 (Presidente Figueiredo, Brazil): Analysis covers E index from Gaite et al. (1997) and structural iron content [Fe^{3+}] in ppm from Balan et al. (2000). Accessory mineral: A: anatase; G: gibbsite.

Sample	Origin	Ac. Min.	HI	LI	E-index	Struct. [Fe^{3+}]
KGa-2	Sediment	A	0.21	0.68	11.3	3000
PF2-50	Soil	A, G	0.17	0.44	17.0	2400

PF2-50 exhibited a lower HI value of 0.17, an LI of 0.44, and an E-index of 17. These indices, commonly used in kaolinite studies, provided insights into the degree of crystalline order at long-range (XRD), whereas EPR assessed local-range disorder. The structural iron concentrations in KGa-2 and PF2-50 were 3000 ppm and 2400 ppm, respectively, as determined using the methodology of Balan et al. (2000). These values, along with the crystalline order indices, hinted at different formation conditions of the kaolinites. Notably, the high concentrations of structural Fe^{3+} in these samples, compared to kaolinites from various origins (Balan et al., 2000), did not directly correlate with the level of structural disorder in kaolinite but were instead expected to be linked with iron, silica, and water activities during crystal growth (Trolard and Tardy, 1989).

3.2 EPR spectra of raw samples

The EPR powder spectra for the PF2-50 and KGa-2 samples displayed characteristic signals typically associated with kaolinite (Fig. 1). The spectra revealed the presence of structural Fe^{3+}, substituting Al^{3+} within the octahedral sites of the kaolinite framework, detectable at lower magnetic fields (Balan et al., 1999). On the spectrum of structural Fe^{3+}, two distinct signals correspond to $Fe_{(1)}$ and $Fe_{(2)}$. The evidenced disorder is mainly related to stacking faults, but the EPR of structural iron also showed sensitivity to point defects in artificially irradiated samples (Gaite et al., 1997). The relative intensity of the $Fe_{(2)}$ signal within the spectra suggested that the KGa-2 sample exhibited a considerably more ordered structure when compared to PF2-50 because the $Fe_{(2)}$ signal was significantly intense. In contrast, for the laterite kaolinite, the $Fe_{(1)}$ signal was dominant (Fig.1). The baseline signal across the spectra is attributed to concentrated iron remaining in the kaolinite particles after deferration, as associated particles of oxides or oxyhydroxides (Muller and Calas, 1993), or as clusters. The total EPR spectra of the natural kaolinite samples displayed the classical signals of RIDs within the magnetic field range of 335 to 365 mT (Fig.1.).

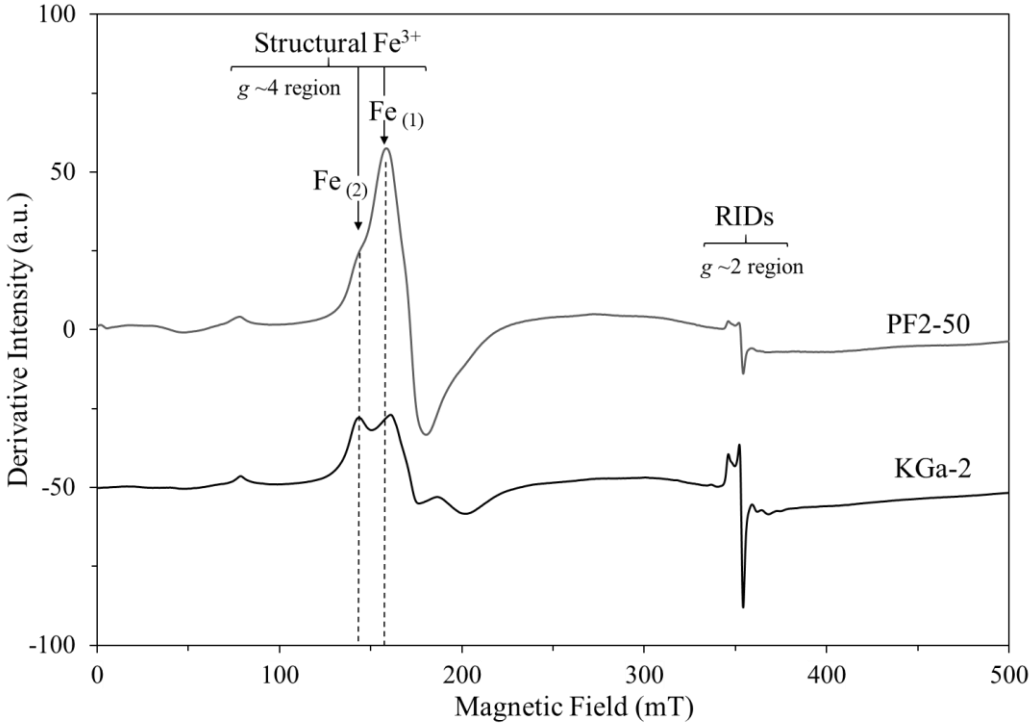

Fig. 1. Normalized total EPR Spectra of kaolinites revealing local crystalline disorder via structural Fe^{3+} (according to relative amplitudes of parts of so-called Fe $_{(2)}$ and Fe $_{(1)}$ signals) alongside a characteristic RIDs signal in the g=2 region. Both samples exhibit contrasting relative intensities of paramagnetic species owing to their natural irradiation conditions.

In the zoomed spectra of radiation-induced defects of kaolinite samples (Fig. 2), a doublet indicative of an apparent axial symmetry in the g tensor was identified, characterized by values for the A-center $g_{//}$=2.049 ± 0.002 and $g_{\perp}$=2.002 ± 0.001 (Clozel et al., 1994). These spectral features were consistent with previous characterizations of the A-center as holes trapped on apical oxygen atoms, commonly referred to as Si-O^- centers, following Marfunin's systematics (Marfunin, 1979).

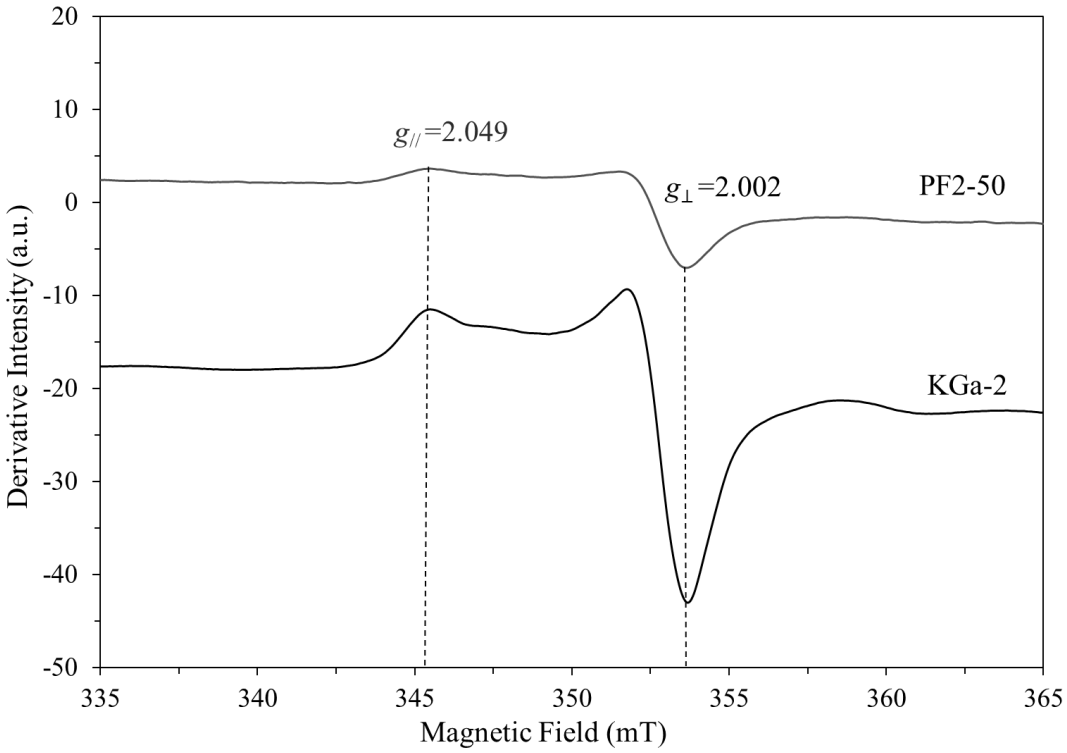

Fig. 2. EPR Spectra of radiation-induced defects in natural samples: The distinct components at $g_{//}$ ~2.049 and $g_{\perp}$ ~2.002 are typical of the A-center in kaolinite.

3.3. Isothermal annealing

3.3.1. Annealing of unstable defects

Artificial irradiations were also found to produce defects in kaolinite that are much less stable than natural A-centers, dominantly annealed at 250°C, 2h, according to Allard et al. (1994). Annealing of unstable defects produced by artificial irradiations before EPR measurement was frequently performed, such as on quartz (Tsukamoto et al., 2018; Benzid and Tani, 2024). Tsukamoto et al. (2018) concluded that heating irradiated samples with appropriate temperature and duration is necessary to match the natural behavior of defects in Al and Ti centers in quartz.

EPR spectra in Figure 3 showed the evolution of defect centers in KGa-2 upon irradiation with two distinct doses, 10^{12} and 10^{13} ions/cm^2 and subsequent heating at 250°C at different annealing durations. Firstly, the typical shape of the A-center, which was by far

dominant, was observed on all spectra. However, comparing the shortest and longest annealing times (2h and 408h) revealed that a minor component was annealed during this time interval. This annealed component was revealed by subtracting the 2h spectrum from the 408h spectrum. The results exhibited an axial signal with a $g_{//}$ component valued at 2.037 ± 0.002, aligning closely with the A' defect characteristics reported by Clozel et al. (1994), where $g_{//}$ was 2.039 ± 0.002. This suggests a significant correlation between the two findings. Thus, the longest annealing impacted a small amount of A' species, leaving the A-centers unaffected. A minor part of the EPR RID spectrum may consist of A's contribution in the conditions (250°C, 2h) used for the dating protocol. However, it was generally observed that the RID signal's shape (not the amplitude) irradiated at different doses and subsequently annealed at 250°C was similar. Therefore, the dominant proportion of A centers remained nearly constant, and consequently, the concentration could be estimated from the signal's amplitude. This presents a relevant simplified approach to avoid the linear decomposition of the signal (Allard et al., 1994; Allard and Muller, 1998), which is more complex and requires a shape for the baseline that is most often unknown with accuracy.

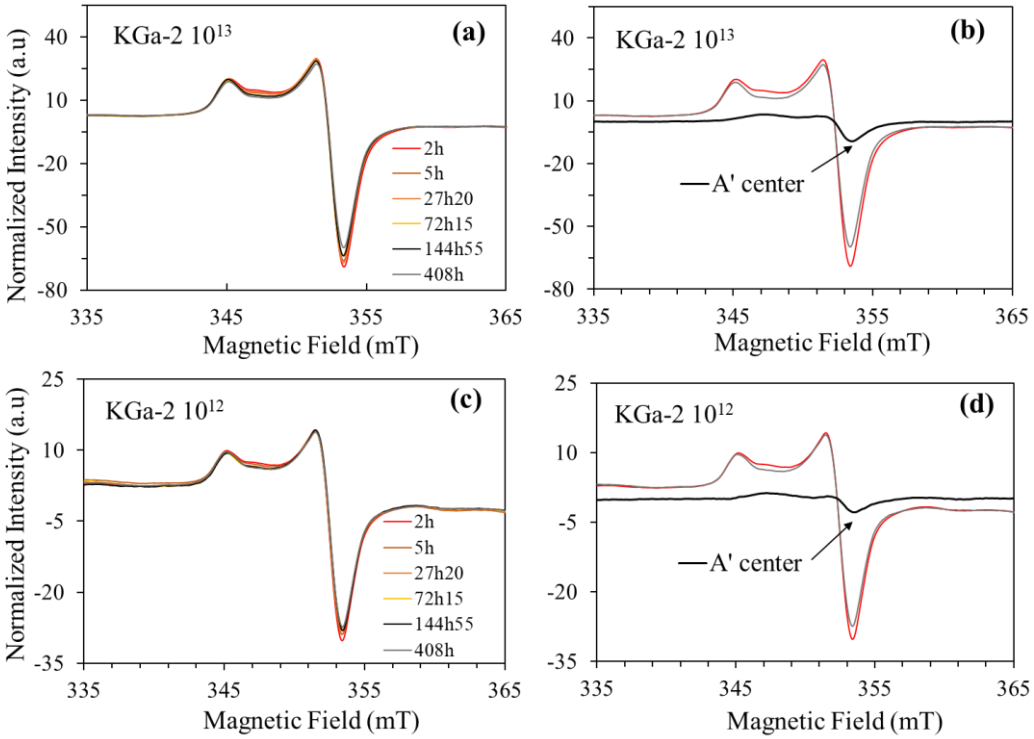

Fig. 3. Annealing effects on KGa-2 samples after irradiation with two distinct doses (spectra of RID overlaid in a, c). In b, d, the difference between the RID spectra after 408 h and 2h heating in bold black line (see the arrow) shows that the annealed species is the A'-center, not the A-center.

Consequently, the 250°C 2h step of annealing after irradiation remains appropriate for the dating protocol.

3.3.2. Annealing of natural and artificial A-centers

3.3.2.1. RID Spectra of KGa-2 and PF2-50

The EPR spectra for the kaolinite samples KGa-2 and PF2-50, which were subjected to both natural and artificial irradiation (at 10^{13} ions/cm^2), are shown in Supplementary Figure 3, over different thermal treatment durations, from 18 to 120 hours at 350- 400°C. This reveals a consistent decline in A-center signal amplitude (Fig. S3). Figure 4 further illustrates that for KGa-2 and PF2-50, the signal intensity progressively decreases over time, peaking at 120 hours, and significantly reduces A-center concentrations at 400°C.

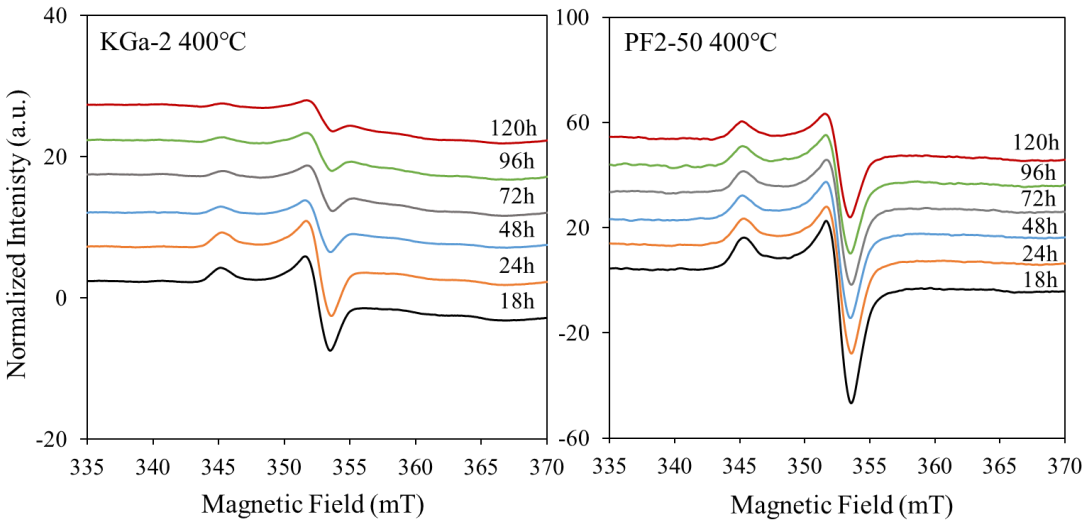

Fig. 4. Normalized EPR Spectra in the g=2 region illustrating the isothermal annealing effect on the amplitude of the signals for KGa-2 and PF2-50. Both natural samples were heated at 250°C for 2h before annealing at 400°C. All these spectra allow the measurement of the A-center concentration from the signal amplitude on the $g_{\perp}$ component without interference.

3.3.2.2. Concentration of the radiation-induced defects

The experimental results revealed several findings regarding the behavior of artificially and naturally irradiated PF2-50 and KGa-2 minerals samples at various temperatures over time (Table 2*)*. Firstly, it was evident, as expected, that artificial irradiation led to a substantially higher initial concentration of RIDs in both PF2-50 and KGa-2 compared to their naturally irradiated counterparts. For instance, after 250°C and 2 hours of annealing, the artificially irradiated PF2-50 exhibited a RID concentration of 44.5 a.u., significantly exceeding the naturally irradiated sample's 7.3 a.u. Similarly, in the same conditions, the KGa-2 sample under artificial irradiation displayed a higher defect concentration (105 a.u.) than the natural sample (28 a.u.).

Table 2. Concentration measurements of radiation-induced defects in natural and artificially irradiated (10^{13} ions/cm^2 fluence indicated) samples, with an error on [RID] of ±10%.

		KGa-2	KGa-2 10^{13}	PF2-50	PF2-50 10^{13}
250°C	2h	28.0	105.0	7.3	44.5
350°C					
	18h	26.2	61.5	6.7	28.1
	24h	25.6	49.0	6.6	23.2
	48h	25.3	44.0	6.5	20.7
	72h	24.2	39.3	6.4	20.2
	96h	23.2	37.0	6.2	19.5
	120h	22.8	30.7	5.8	18.9
375°C					
	18h	18.6	55.5	7.1	11.1
	24h	17.1	50.0	5.3	9.6
	48h	14.0	34.4	4.4	7.4
	72h	13.0	25.0	4.1	6.0
	96h	10.0	18.0	3.5	5.4
	120h	9.0	14.2	3.0	5.0
400°C					
	18h	9.6	13.8	4.1	6.9
	24h	8.6	10.0	3.4	6.2
	48	4.6	5.8	2.2	3.8
	72h	3.4	3.8	1.8	3.1
	96h	2.7	2.8	1.5	2.6
	120h	2.0	2.1	1.3	2.2

Additionally, all the concentrations of RIDs decreased with time, whatever the temperature, confirming that the thermal conditions for annealing were fulfilled. The results

299 also highlighted a notable distinction between the two minerals, with KGa-2 consistently
300 exhibiting a higher concentration of RIDs than PF2-50 under similar conditions. As the [RID]
301 is known to increase with the dose of ionizing radiation (Allard et al., 1994; Allard and
302 Muller, 1998), this discrepancy might be attributed to inherent differences in the dose
303 experienced by these minerals in their environment due to a combined effect of age and dose
304 rate. Nevertheless, other factors might also be considered, such as the amount and type of
305 existing electron-hole traps in their structure (Ikeya, 1993). Such traps for electron holes are
306 expected to arise from oxygen interstitials or oxygen ions near a divalent impurity occurring
307 in the kaolinite structure, according to the model of A-center proposed by Angel et al. (1974).
308 By restoring the local charge balance, this model accounts for the high stability of this
309 paramagnetic species. In addition, the two samples may also differ concerning the kinetics of
310 RID formation, which was shown to be sample-dependent (e.g., Allard et al., 1994; Allard
311 and Muller, 1998; Mathian et al., 2020). However, the RID growth curves can only be
312 revealed by irradiations at various doses and by the analysis of resulting dosimetry curves
313 (e.g., Allard and Muller, 1998), which is out of the scope of this study.
314
315 3.3.2.3. Stability of A-center

316 Temperature-dependent decay kinetics were experimentally investigated by isothermal
317 annealing, which allows the assessment of parameters such as half-life and activation energy
318 (E_a). The decay processes are classically described by first or second-order equations (Furetta,
319 1988). This permits the calculation of half-life at room temperature by extrapolating high-
320 temperature parameters. Such isothermal heating experiments were previously performed on
321 natural radiation-induced defects of reference kaolinites (Clozel et al., 1994) but not on
322 artificially produced defects. The related equations are as follows:

323 The first order law can be written:

$$[A] = [A_0]\, e^{-Kt} \qquad \text{[eq. 2]}$$

Where [A] is the defect concentration (a.u.), [A_0] is the initial concentration, t is the time of decay, and K is the probability of decay per second, which can be expressed as:

$$K = (t_{1/2})^{-1} \times \ln 2 = s_0 \times e^{-Ea/kT} \qquad \text{[eq. 3]}$$

s_0 is the frequency factor in the unit of per second (s^{-1}), k is the Boltzmann constant (k= 8.6×10^{-5} eV K^{-1}), and T is the temperature (K). From relation (eq. 2-3), it can be seen that with first-order kinetics, the half-life is only temperature dependent and that at least two isotherm curves are required to determine E_a.

More complex mechanisms may occur with second-order decay law, involving re-trapping in the decay process:

$$[A]^{-1} = K \times t + [A_0]^{-1} \qquad \text{[eq. 4]}$$

and

$$K = \text{tg}\,\theta = (t_{1/2} \times [A_0])^{-1} = s_0 \times e^{-Ea/kT} \qquad \text{[eq. 5]}$$

or

$$\ln K = \ln s_0 - (Ea/k) \times T^{-1} \qquad \text{[eq. 6]}$$

Where θ is the slope of the linear curve (eq. 4), it should be noticed that for second-order kinetics, the concept of half-life is a temperature and time-dependent function of [A_0]. Values of K can be calculated at different temperatures from (eq. 4) and the constants E_a, s_0 by fitting the linear expression of T^{-1} in (eq. 6).

Figure 5 illustrates the isothermal annealing process of the A-center in kaolinite for both KGa-2 and PF2-50 samples at three distinct temperatures: 400°C, 375°C, and 350°C. The KGa-2 sample demonstrated a linear increase in the 1/[A] ratio overtime at all temperatures, clearly expressed at 400°C. This linear trend was also observable for the KGa-2

10^{13} ions/cm^2 variant, albeit at a slightly attenuated rate. The PF2-50 samples showed similar temperature-dependent patterns but were displayed at different scales.

The linear representations of the 1/[*A*] isotherm indicated that the decay law was described by second-order kinetics.

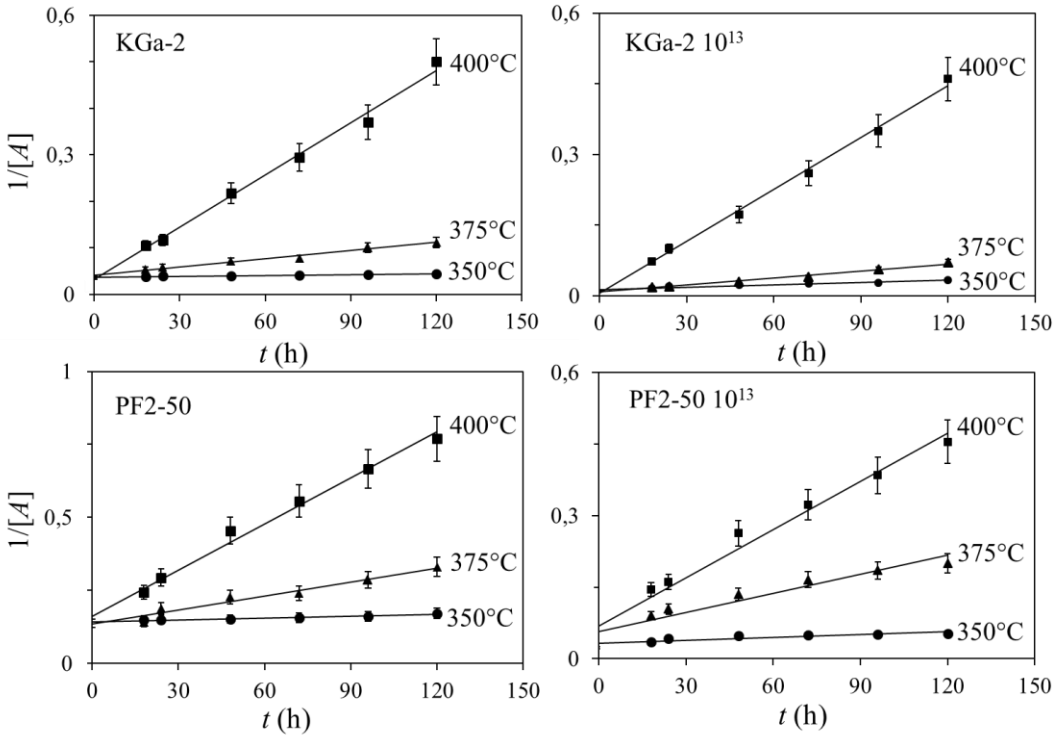

Fig. 5. Isothermal annealing of A-centers at different temperatures for KGa-2 and PF2-50 samples. Kinetics corresponds to second-order laws, according to the linear increase of 1/[*A*] as a function of time.

3.3.2.2. Kinetic parameters

Utilizing a 1/[*A*] representation allowed the determination of the temperature-dependent decay constant *K*, which was the slope of the linear curves represented in Fig. 5 (Table 3).

Table 3. The decay parameters were derived from the thermal annealing on natural and artificially irradiated samples (10^{13} ions/cm^2 fluence indicated). The 300K values were extrapolated.

		K (decay per second) ±10%			
T (°C)	T (K)	KGa-2	KGa-2 10^{13}	PF2-50	PF2-50 10^{13}
400	673	0.0037	0.0037	0.0053	0.0034

375	648	0.0006	0.0005	0.0016	0.0013
350	623	0.0001	0.0002	0.0002	0.0002
27	300	1.89×10^{-27}	8.93×10^{-23}	4.64×10^{-25}	2.89×10^{-22}

Subsequently, ln*K* values were inferred, allowing for the determination of s_0 and activation energy using Eq .6. The relation between ln*K* and 1/*T* for the three experimental temperatures was linear (Figure 6). This allowed the extrapolation of ln*K* and K to 300K (Tables 4, 3).

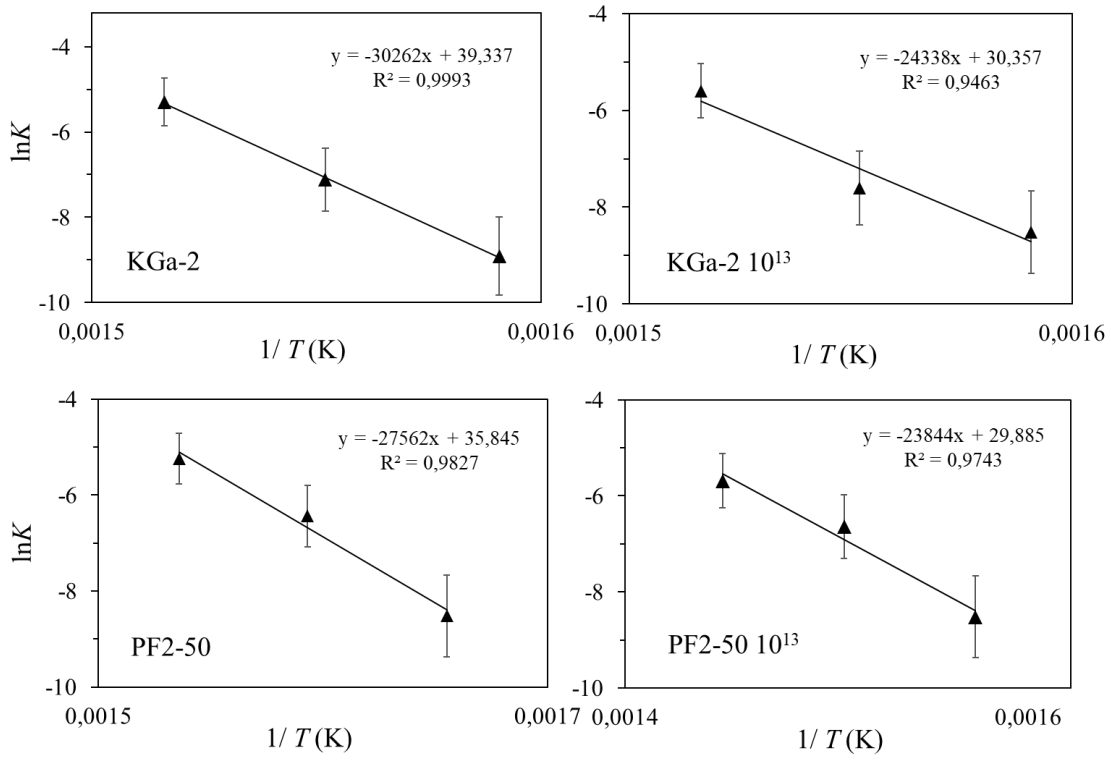

Fig.6. Correlation between the natural logarithm of the decay constant *K* considering ±10% error on (ln*K*) and the inverse temperature (1/*T*) for both the KGa-2 and PF2-50 samples. The linear equations allow extrapolations of ln*K* to 300K.

Although only three experimental points were available, the linear fit had good R^2 values, affirming the reliability of the second-order annealing process.

Table 4 provides an insightful overview of the reaction kinetics parameters, focusing on the activation energy, the half-life $t_{1/2,}$ and the frequency factor s_0 at room temperature.

The KGa-2 and PF2-50 samples displayed activation energies (E_a) ranging from 2 to 2.6 eV and 2 to 2.3 eV, respectively, with an estimated error of ±20% based on second-order kinetic principles applied to the ln$K$ versus 1/T plot. These values of activation energy were higher than those generally reported for defects in other minerals, such as quartz by TL or OSL (e.g., Schmidt et al., 2018) or by EPR (Toyoda and Ikeya, 1991; Nilges et al. 2008, 2009; Pan et al., 2008; Pan and Hu, 2009; Benzid and Tani, 2024). Nevertheless, they remained close to those determined for natural A-centers in kaolinite by Clozel et al. (1994), i.e., 2 eV. Even considering the error in their value, there were systematically higher for the naturally produced defects when compared to their artificial counterparts. Indeed, as the decay process was a second-order kinetics, the concentration of RIDs, consistently higher for the artificially irradiated kaolinites, was expected to influence the stability parameters. Some studies of the stability of radiation-induced defects such as [AlO_4/h^+] and [TiO_4/M^+] in quartz, where M^+ is usually H^+ or alkali ions, have shown an evolution of the activation energy as a function of the dose that varied in the same direction as those revealed herein for kaolinite: the higher the dose, the lower the activation energy (Benzid and Gabor, 2020).

The ±20% error in $t_{1/2}$ was calculated from Eq .5. using extreme K decay constant values. The error in s_0, estimated from Eq. 6 with extreme values of LnK and E_a, extends to several orders of magnitude (up to ~108) as it arises from a logarithmic expression.

Table 4. Kinetic parameters for artificial and natural defects with error values (with the ±20% error in $t_{1/2}$ and the ±20% error in E_a, along with several orders of magnitude for s_0).

300K (27°C)	KGa-2		PF2-50	
	Natural	Irradiated	Natural	Irradiated
E_a (eV)	2.60	2.09	2.37	2.05
s_0 (s^{-1})	1.2×10^{17}	1.5×10^{13}	3.6×10^{15}	9.5×10^{12}

$t_{1/2}$ (yrs)	6.0×10^{17}	3.4×10^{12}	9.3×10^{15}	2.4×10^{12}

The s_0 (frequency factor) value for KGa-2 is 1.21×10^{17}, and for KGa-2 10^{13} ions/cm^2 it was 1.52×10^{13} s^{-1}. Similarly, for PF2-50, s_0 values of 3.69×10^{15} and 9.52×10^{12} s^{-1} were observed for PF2-50 at a fluence of 10^{13} ions/cm^2. These obtained values were orders of magnitude higher than the one mentioned by Marfunin (1979), which, according to this author, is expected to be around 10^{10} s^{-1}. However, for the 110°C TL peak of another silicate, such as quartz, Schmidt et al. (2018) reported frequency factors derived from isothermal decay analyses in an interlaboratory experiment that ranged from 10^6 to 10^{17} s^{-1}, depending on the heating rates and measurement systems used. Several authors using TL or OSL of quartz found frequency factors exceeding 10^{14} s^{-1} (Minelli et al., 2021; Veronese et al., 2004a). In their literature review of the parameters of quartz TL glow peaks, Veronese et al. (2004b) cited several values reaching 10^{14} s^{-1} (see their Table 1) and two even surpassing 10^{16} s^{-1} (Chruscinska et al., 1996; Kaipa and Haskell, 1985). Thus, these findings of high values of frequency factors for quartz support the relatively high s_0 values observed in this study. The work by Benzid and Gabor (2020) also demonstrated for [AlO_4/h^+] and [TiO_4/M^+] in quartz that there is a positive coevolution of activation energy with the frequency factor as a function of dose. Such an evolution was also observed for KGa-2 and PF2-50. However, this study included only two doses (natural and artificial), contrary to the aforementioned authors, who concluded that their data set follows a Meyer-Neldel rule.

Clozel et al. (1994) documented half-life for natural A-centers as above 10^{12} years. Such a prolonged half-life established kaolinite as a robust option for radiation dosimetry, especially under the low thermal constraints at the Earth's surface (considered herein as circa 300K). The findings, correlating with the work of Clozel et al. (1994), revealed half-lives estimated to be greater than 10^{12} years at room temperature, reinforcing the adopted methodology and its potential implications for future research in geological radiation

dosimetry. In contrast to first-order kinetics, the half-life derived from second-order kinetics was not constant and depended on the initial concentration of defects (and temperature). Thus, one significant dataset observation was the difference in half-life values between natural and irradiated samples. Given the principles of second-order kinetics, a rise in the initial concentration invariably shortened the half-li IEq. 5) to keep the *K* value constant. This suggests that the decay process may be sensitive to the closeness of defects in the kaolinite structure. The artificial defect centers, whose concentration was much higher than naturally produced ones, had thus minimum and very high half-lives. They emerged as remarkably stable, reinforcing the methodology for using A-centers of kaolinite as a geochronometer of the geosphere. Nevertheless, it is noticed that higher temperatures of formation and evolution of kaolinites, e.g., in hydrothermal systems, would significantly anneal the A-centers, which would require constraints on the thermal regime of the system vs time to use these defects as geochronometers.

The nature of A-centers can improve the understanding of their exceptionally high stabilities. Indeed, two models were proposed by Angel et al. (1974). The first one was a hole on apical oxygen in the vicinity of a divalent substitution (e.g., Mg^{2+} substituting for Al^{3+}). Once an electron has been removed from this oxygen by ionizing radiations, the O^- anion becomes paramagnetic (electronic structure He $2s^2\ 2p^5$) and above all, the local mass balance is restored. This is typically a process of decoration close to an impurity precursor. The second model was an electron hole on a peroxy molecule that becomes O_2^-, but the location of the interstitial oxygen in the kaolinite structure is not yet known. It is known that the electron resides in a π orbital (Angel et al., 1974), and its orientation, as inferred from the $g_{//}$ component, is perpendicular to the (ab) plane (Clozel et al., 1994). Both these models are consistent with the long stability of the A-center, mainly if the peroxy occurs near the heterovalent substitution. However, nothing is known so far about the species that capture the ejected electrons nor the local structure before irradiation: it might involve a compensation by

a small interstitial cation that diffused away because of the hole formation, as was proposed for some RIDs in quartz (e.g., Benzid and Gabor, 2020). In addition, the trivalent structural iron is a good candidate for electron capture, but this has not yet been demonstrated. Indeed, the EPR spectrum in the g=4 region broadened and increased with dose as a narrow signal, which is inconsistent with a reduction. Still, the identity of the growing narrow signal remained obscure. It was proposed by Worasith et al. (2018) that it corresponds to a triplet state related to RIDs, thus interfering with the iron signal. This is likely, and according to Gaite et al. (1997), it might be correlated to the growth of B-centers during irradiation that was shown to influence the g=4 signal as the width of the structural iron spectrum and as the intensity of the narrow signal.

4. Conclusion

The findings reveal comparisons between the thermally assisted decay kinetics of natural and artificial A-centers in kaolinite. Utilizing a second-order reaction model instead of a first-order one provided a much more accurate representation of the annealing kinetics. All the activation energies were discerned between 2.0 and 2.6 eV for the reference and irradiated samples. Remarkably, extrapolated half-life values of artificially generated A-centers, assessed at room temperature, are consistent with previous research on naturally induced kaolinite defects, as they exceed 10^{12} years. In conclusion, the results affirm that artificially generated A-centers simulate natural ones in terms of EPR signal and stability, thereby validating and fortifying their use in advanced EPR dating methodologies of kaolinites.

Declaration of Competing Interest

The authors declare that they have no known competing financial interests or personal relationships that could have influenced the work reported in this paper.

Acknowledgments

The sample PF50 has been collected in the framework of the French funding Agency ANR RECA-ANR-17-CE01-0012-01 project. We thanked the participants of the field trip, D. Calmels, D. Guinoiseau, and Z. Fekiacova. The authors would like to acknowledge the scientific team of the Aramis linear accelerator particles in Orsay (France). Moreover, we are grateful for the support and help given to this work by the EPR and X-ray spectroscopy platform of the IMPMC at Sorbonne Université, France.

Appendix A. Supplementary data

Supplementary data to this article can be found online.

References

Allard, T., Muller, J.-P., Dran, J.C., Ménager, M.T., 1994. Radiation-induced paramagnetic defects in natural kaolinites: alpha dosimetry with ion beam irradiation. Phys. Chem. Miner. 21, 85–96. https://doi.org/10.1346/CCMN.1997.0450402.

Allard, T., Muller, J.P., 1998. Kaolinite as an in situ dosimeter for past radionuclide migration at the Earth's surface. Appl. Geochem. 13, 751-765. https://doi.org/10.1016/S0883-2927(98)00011-0

Allard T., Ildefonse, P., Calas, G., 2007. Reconstruction of past uranium migration in a sedimentary deposit (Coutras, France): implications for a radwaste repository. Chem Geol. 239, 50-63. https://doi.org/10.1016/j.chemgeo.2006.12.007.

Allard, T., Calas, G., 2009. Radiation effects on clay mineral properties. Appl. Clay Sci. 43, 143-149. https://doi.org/10.1016/j.clay.2008.07.032.

Allard, T., Balan, E., Calas, G., Fourdrin, C., Morichon, E., Sorieul, S., 2012. Radiation-induced defects in clay minerals: a review. Nucl Instrum Methods. 277, 112-120. https://doi.org/10.1016/j.nimb.2011.12.044.

Allard, T., Gautheron, C., Bressan Riffel, S., Balan, E., Soares, B. F., Pinna-Jamme, R., 2018. Combined dating of goethites and kaolinites from ferruginous duricrust. Deciphering the

Late Neogene erosion history of Central Amazonia. Chem Geol. 479, 136-150. https://doi.org/10.1016/j.chemgeo.2018.01.004.

Allard, T., Pereira, L., Mathian, M., Balan, E., Taitson Bueno, G., Falguères, C., Do Nascimento, N., 2020. Dating kaolinite from the Neogene Içà Formation and overlying laterites, central Amazonia, Brazil: constraints for a stratigraphic correlation. Palaeogeogr Palaeocl. 554, 1-15. https://doi.org/10.1016/j.palaeo.2020.109818.

Angel, B.R., Jones, P.E. J., Hall, P. U., 1974. Electron spin resonance studies of doped synthetic kaolinite I. Clay Miner. 10, 247-255. https://doi.org/10.1180/claymin.1974.010.4.03.

Balan, E., Allard, T., Boizot, B., Morin, G., Muller, J.P., 1999. Structural Fe^{3+} in natural kaolinites: new insights from electron paramagnetic resonance spectra fitting at X and Q-band frequencies. Clays Clay Miner. 47, 605-616. https://doi.org/10.1346/CCMN.1999.0470507.

Balan, E., Allard, T., Boizot, B., Morin, G., Muller, J.P., 2000. Quantitative measurement of paramagnetic Fe^{3+} in kaolinite. Clay Clay Miner. 48, 439-445. https://doi.org/10.1346/CCMN.2000.0480404.

Balan, E., Allard, T., Fritsch, E., Selo, M., Falguères, C., Chabaux, F., Pierret, M.-C., Calas, G., 2005. Formation and evolution of lateritic profiles in the middle Amazon basin: insights from radiation-induced defects in kaolinite. Geochim Cosmochim Ac. 69, 2193-2204. https://doi.org/10.1016/j.gca.2004.10.028.

Balan, E., Fritsch, E., Allard, T., Morin, G., Guillaumet, M., Delattre S., Blanchard, M., Calas, G., 2011. Spectroscopic investigation and theoretical modeling of kaolinite-group minerals and other low-temperature phases, C. R. Geoscience. 343. https://doi.org/10.1016/j.crte.2010.10.006.

Balan, E., Calas, G., Bish, D.L., 2014. Kaolin group minerals: from hydrogen-bonded layers to environmental recorders. Elements. 10, 183-188. https://doi.org/10.2113/gselements.10.3.183.

Benzid, K., Gabor, A.T., 2020. The compensation effect (Meyer-Neldel rule) on [AlO4/h^+] and [TiO4/M^+] paramagnetic centers in irradiated sedimentary quartz. AIP Adv. 10, 75-114. https://doi.org/10.1063/5.0005161.

Benzid, K., Tani, A., 2024. Thermal behavior of E′ point defects in gamma-irradiated natural quartz: Study of the Meyer-Neldel rule using electron spin resonance. J Lumin. 265, 01-08. https://doi.org/10.1016/j.jlumin.2023.120218.

Cases, J. M., Liétard, O., Yvon, J., Delon, J. F., 1982. Etude des propriétés cristallographiques, morphologiques, superficielles de kaolinites désordonnées. Bull Minéral. 105, 439-455.

Chruscinska, A., Oczkowski, H.L., Przegietka, K.R., 1996. Trap spectra of annealed quartz. Acta Phys Pol. 89, 55-568. https://doi.org/10.12693/APhysPolA.89.555.

Clozel, B., Gaite, J.-M., Muller, J.P., 1994. Al-O-Al paramagnetic defects in kaolinite. Phys Chem Miner. 22, 352-356. https://doi.org/10.1007/BF00213331.

Cuttler, A. H., 1980. The behavior of a synthetic 57Fe-doped kaolin; Mössbauer and electron paramagnetic resonance studies. Clay Miner. 15, 429-444. https://doi.org/10.1180/claymin.1980.015.4.10.

Furetta, C., 1988. New calculations concerning the fading of thermoluminescent materials. Nucl. Tracks Radiat Meas. 14, 413-414. https://doi.org/10.1016/1359-0189(88)90018-0.

Gaite, J.M., Ermakoff, P., Muller, J.P., 1993. Characterization and origin of two Fe^{3+} EPR spectra in kaolinite. Phys Chem Miner. 20, 242-247. https://doi.org/10.1007/BF00208137.

Gaite, J.M., Ermakoff, P., Allard, T., Muller, J.P., 1997. Paramagnetic Fe^{3+}: a sensitive probe for disorder in kaolinite. Clays Clay Miner. 45, 496-505. https://doi.org/10.1346/CCMN.1997.0450402.

Giese, R.F., 1988. Kaolin minerals: structures and stabilities. In: Bailey, S.W. (Eds.), Hydrous Phyllosilicates. Mineralogical Society of America, Washington D.C., pp. 29-66. https://doi.org/10.1515/9781501508998-008.

Goodman, B. A., Worasith, N., Deng, W., 2016. EPR spectra of a new radiation-induced paramagnetic centre in kaolins. Clay Miner. 51(5), 707–714. https://doi.org/10.1180/claymin.2016.051.5.01

Hennig, G.J., Grün, R., 1983. ESR dating in quaternary geology. Quat. Sci. Rev. 2, 2-3, 157-238. https://doi.org/10.1016/0277-3791(83)90006-9.

Hinckley, D.N., 1962. Variability in crystallinity values among the kaolin deposits of the coastal plain of Georgia and South Carolina. Clays Clay Miner. 11, 229-235. https://doi.org/10.1346/CCMN.1962.0110122.

Ildefonse, P., Muller, J.P., Clozel, B., Calas, G., 1990. Study of two alteration systems as natural analogs for radionuclide release and migration. Eng. Geol. 29, 413-439. https://doi.org/10.1016/0013-7952(90)90076-D.

Kaipa, P.L., Haskell, E.H., 1985. In situ dosimetry using the sensitized 210°C TL peak of quartz. Nucl Tracks, 10, 621-623. https://doi.org/10.1016/0735-245X(85)90067-5.

Liétard, O., 1977. Contribution à l'étude des propriétés physico-chimiques,cristallographiques et morphologiques des kaolins, PhD Thesis, Institut national polytechnique de Lorraine, Nancy, 345p.

Marfunin, A.S., 1979. Spectroscopy, Luminescence, and Radiation Centers. In: Minerals. Schiffer, V.V. (Eds), Springer Verlag, Heidelberg, pp. 352. https://doi.org/10.1180/minmag.1980.043.330.28.

572 Mathian, M., Aufort, J., Braun, J.J., Riotte, J., Selo, M., Balan, E., Fritsch, E., Bhattacharya,
573 S., Allard, T., 2019. Unraveling weathering episodes in Tertiary regoliths by kaolinite
574 dating (Western Ghats, India). Gondwana Res. 69, 89-105.
575 https://doi.org/10.1016/j.gr.2018.12.003.
576 Mathian, M., Taitson Bueno, G., Balan, E., Fritsch, E., Nascimento, Selo, M., Allard, T.,
577 2020. Kaolinite dating from Acrisol and Ferralsol: a new key to understanding the
578 landscape evolution in NW Amazonia (Brazil). Geoderma, 370, 01-18.
579 https://doi.org/10.1016/j.geoderma.2020.114354.
580 Mathian, M., Chassé, M., Calas, G., Griffin, W.L., O'Reilly, S.Y., Buisson, T., Allard, T.,
581 2022. Insights on the Cenozoic climatic history of southeast Australia from kaolinite
582 dating. Palaeogeogr Palaeocl. 604, 01-12. https://doi.org/10.1016/j.palaeo.2022.111212.
583 Meads, R. E., Malden, P. J., 1975. Electron spin resonance in natural kaolinites containing Fe
584 and other transition metal ions. Clay Min. 10, 313-345.
585 https://doi.org/10.1180/claymin.1975.010.5.01.
586 Mehra, O.P., Jackson, M.L., 1960. Iron oxide removal from soils and clays by a dithionite-
587 citrate system buffered with sodium bicarbonate. Clays Clay Miner. 7, 317-327.
588 https://doi.org/10.1016/B978-0-08-009235-5.50026-7.
589 Minelli, T.D., Sawakuchi, A.O., Guralnik, B., Lambert, R., Jain, M., Pumim, F.N., de Rio, I.,
590 Guedes, C.C.F., Nogueira, L., 2021. Variation of luminescence sensitivity characteristic
591 dose and trap parameters of quartz from rocks and sediments. Radiat. Meas. 1444, 01-10.
592 https://doi.org/10.1016/j.radmeas.2021.106583.
593 Muller, J.P., Calas, G., 1989. Tracing kaolinites through their defect centers; kaolinite
594 paragenesis in a laterite (Cameroon). Econ. Geol. 84, 694-707.
595 https://doi.org/10.2113/gsecongeo.84.3.694.

Muller, J.P., Clozel, B., Ildefonse, P., Calas, G., 1992. Radiation-induced defects in kaolinite: Indirect assessment of radionuclide migration in the geosphere. Appl. Geochem. 1, 205-216. https://doi.org/10.1016/S0883-2927(09)80077-2.

Muller, J.P., Calas, G., 1993. Genetic significance of paramagnetic centers in kaolinites. In: Murray, H.H., Bundy, W., Harvey, C. (Eds.) Kaolin genesis and utilization. The Clay Minerals Society, Boulder, Colorado, pp. 261-289. https://doi.org/10.1346/CMS-SP-1.13.

Murray, H.H., 1988. Kaolin minerals: their genesis and occurrences. In: Bailey., S.W. (Eds.). Hydrous phyllosilicates, reviews in mineralogy. Washington, D.C.: Mineralogical Society of America, 67-90. https://doi.org/10.1515/9781501508998-009.

Murray, H.H., 2007. Applied clay mineralogy: Occurrence, processing, and application of kaolins, bentonites, palygorskite-sepiolite, and common clays. Clays Clay Miner. 55, 644–645. https://doi.org/10.1007/BF03406033.

Nilges, M.J., Pan, Y., Mashkovtsev, R.I., 2008. Radiation-induced defects in quartz. I. Single-crystal W-band EPR study of an electron irradiated quartz. Phys Chem Miner. 35, 103-115. https://doi.org/10.1007/s00269-007-0203-5.

Pan, Y., Nilges, M.J., Mashkovtsev, R.I., 2008. Radiation-induced defects in quartz. II. Single-crystal W-band EPR study of a natural citrine quartz. Phys. Chem. Miner. 35, 387-397. https://doi.org/10.1007/s00269-008-0233-7.

Pan, Y., Hu, B., 2009. Radiation-induced defects in quartz. IV. Thermal properties and implications. Phys. Chem. Miner. 36, 421-430. https://doi.org/10.1007/s00269-009-0288-0.

Pineau, M., Mathian, M., Baron, F., Rondeau, B., Le Deit, L., 2022. Estimating kaolinite crystallinity using near-infrared spectroscopy: implications for its geology on Earth and Mars. Amer. Miner. 107, 1453-1469. https://doi.org/10.2138/am-2022-8025.

Plötze, M., Kahr, G., Hermanns Stengele, R., 2003. Alteration of clay minerals: gamma irradiation effects on physico-chemical properties. Appl. Clay Sci. 23, 195-202. https://doi.org/10.1016/S0169-1317(03)00103-0.

Pushkareva, R., Kalinichenko, E., Lytovchenko, A., Pushkarev, A., Kadochnikov, V., Plastynina, M., 2002. Irradiation effect on physico-chemical properties of clay minerals. Appl. Clay Sci. 21, 117-123. https://doi.org/10.1016/S0169-1317(01)00097-7.

Schmidt, C., Friedrich, J., Adamiec, G., Chruścińska, A., Fasoli, M., Kreutzer, S., Martini, M., Panzeri, L., Polymeris, G. S., Przegiętka, K., Valla, P. G., King, G. E., Sanderson, D. C. W., 2018. How reproducible are kinetic parameter constraints of quartz luminescence? An inter laboratory comparison for the 110 °C TL peak. Radiat. Meas. 110, 14-24. https://doi.org/10.1016/j.radmeas.2018.01.002.

Toyoda, S., Ikeya, M., 1991. Thermal stabilities of paramagnetic defect and impurity centers in quartz; basis for ESR dating of thermal history. Geochem. J. 25, 437-445. https://doi.org/10.2343/geochemj.25.437.

Trolard F., Tardy, Y., 1989. A model of Fe^{3+}-Kaolinite, Al^{3+}-Goethite, Al^{3+}-Hematite equilibria in laterites. Clay Miner. 24, 01-21. https://doi.org/10.1180/claymin.1989.024.1.01

Tsukamoto, S., Long, H., Richter, M., Li, Y., King, G.E., Zhong, H., Yang, L., Zhang, J., Lambert, R., 2018. Quartz natural and laboratory esr dose response curves: a first attempt from Chinese loess. Radiat. Meas. 120, 137-142. https://doi.org/10.1016/j.radmeas.2018.09.008.

Van Olphen, H. and Fripiat, J.J., 1979. Data Handbook for Clay Materials and other non-metallic minerals. Pergamon Press, Oxford. https://doi.org/10.1097/00010694-198101000-00013.

644 Veronese, I., Giossani, A., Göksu, H.Y., Martini, M., 2004a. The trap parameters of electrons
645 in intermediate energy levels in quartz. Radiat Meas. 38, 743-746.
646 https://doi.org/10.1016/j.radmeas.2004.01.012.
647 Veronese, I., Giossani, A., Göksu, H.Y., Martini, M., 2004b. Isothermal decay studies of
648 intermediate energy levels in quartz. Radiat Environ Biophys. 43, 51-57.
649 https://doi.org/10.1007/s00411-004-0228-9
650 Worasith, N., Goodman, B.A., Deng, W., 2018. Formation on new low field signals in the
651 EPR spectra of kaolin minerals. J. Appl. Sci. 17, 1, 12-18.
652 https://doi.org/10.14416/j.appsci.2018.05.002.
653 Ziegler, J.F., Ziegler, M.D., Biersack, J.P., 2010. SRIM-The stopping and range of ions in
654 matter. Nucl Instrum Methods. 264, 01-08. https://doi.org/10.1016/j.nimb.2010.02.091.